J Nanopart Res (2012) 14:1130
DOI 10.1007/s11051-012-1130-z

RESEARCH PAPER

A facile synthetic route toward air-stable magnetic nanoalloys with Fe–Ni/Fe–Co core and iron oxide shell

Alexios P. Douvalis · Radek Zboril · Athanasios B. Bourlinos · Jiri Tucek · Stavroula Spyridi · Thomas Bakas

Received: 24 April 2012 / Accepted: 10 August 2012 / Published online: 31 August 2012

Abstract Air-stable bimetallic spherically shaped Fe–Ni and Fe–Co magnetic nanoparticles (MNPs), having an average size of 15 nm and core–shell structure, were synthesized by a simple wet chemical method under ambient conditions. For the first time, sodium borohydride reduction method, commonly applied for the syntheses of metal nanoparticles, was used for the preparation of well-defined Fe–Ni and Fe–Co nanoalloys, avoiding exploitation of any organic solvent. This approach allows a large scale production of nanoparticles specifically stabilized by an iron oxyhydroxide shell without a need of secondary functionalization. Transmission electron microscopy, X-ray powder diffraction, X-ray fluorescence, magnetization, and Mössbauer data demonstrate a core–shell nature of the as-synthesized nanoparticles. The nanoparticle core is of metallic origin and is inhomogeneous at the atomic level, consisting of iron-rich and iron-poor alloy phases. The composition of the shell is close to the ferrihydrite and its role lies in prevention of oxidation-induced degradation of nanoparticle properties. The core is ferromagnetic at and below room temperature, experiencing superparamagnetic relaxation effects due to a reduced size of nanoparticles, whereas the shell is completely superparamagnetic at 300 K and magnetically orders below ~25 K. Both developed types of magnetic nanoalloys exhibit a strong magnetic response under applied magnetic fields with a high magnetization values achievable at relatively low applied magnetic fields. Beside this, the highly biocompatible chemical composition of the nanoparticle shell and ability of its chemical modification by substitution or addition of other ions or molecules further empower the application potential of these MNPs, especially in the field of biomedicine.

Keywords Magnetic nanoparticles · Core–shell · Borohydride · Ferrihydrite · Mössbauer spectroscopy · Magnetization measurements

A. P. Douvalis (✉) · A. B. Bourlinos · S. Spyridi · T. Bakas
Physics Department, University of Ioannina, 45110 Ioannina, Greece
e-mail: adouval@uoi.gr

R. Zboril (✉) · J. Tucek
Regional Centre of Advanced Technologies and Materials, Departments of Physical Chemistry and Experimental Physics, Faculty of Science, Palacky University, Slechtitelu 11, 78371 Olomouc, Czech Republic
e-mail: zboril@prfnw.upol.cz

S. Spyridi
Department of Materials Science and Engineering, University of Ioannina, 45110 Ioannina, Greece

Introduction

Metallic or ceramic magnetic nanoparticles are important materials for a large variety of contemporary and future technological applications, including high-density magnetic recording media (Kodama 1999;

Sun et al. 2000; Skumryev et al. 2003; Hoinville et al. 2003), catalysts (Sinfelt 1983), magnetic fluids (Rheinlander et al. 2000), drug identification and delivery, as well as contrast and hyperthermia agents in biomedicine (Kodama 1999; Berry and Curtis 2003; Pankhurst et al. 2003). Among these nanomaterials, bimetallic Fe–Co and Fe–Ni nanoalloys raise a significant attention due to their application—promising magnetic properties that can be easily tuned by varying composition of individual metals in the system (He et al. 1997; Jang et al. 2004). In the case of Fe–Co nanoalloys, it is well known that Co exhibiting the largest positive magnetic anisotropy enhances the coercive field and residual magnetization of these nanomaterials as its content increases (Li et al. 1998). Fe–Co is generally regarded as a soft magnetic alloy with a high Curie temperature (>1,100 K), high saturation magnetization (>220 emu/g), large magnetic permeability, and low magnetic anisotropy (Poddar et al. 2004). These features predestinate Fe–Co to be exploited in high-temperature applications such as magnetic bearings for high-speed motors, flywheels, gas turbine engines, etc. (Chu et al. 1999). Recently, Fe–Co nanoparticles have been found as components of microwave absorbing materials (for waveguides, modulators, switches) as they show a strong absorption of electromagnetic waves in the gigahertz region driven by high microwave permeability and finite-size effect (Nie et al. 2007; Kim et al. 2004). Thus, they appear to be alternatives to ferrites, commonly employed in the field of electromagnetic shielding, as their microwave permeability dramatically fades away in the high-frequency region due to the Snoek's limit (Sugimoto 1999). Beside this, owing to their eminent magnetic properties, Fe–Co MNPs generate the maximum specific loss power heat per unit mass of MNPs achievable by any (nano)material, strengthening their potential for utilization in thermotherapy treatments (Habib et al. 2008). Fe–Ni nanoalloy displays similar material's characteristics; in addition, it possesses almost zero magnetostriction and significant anisotropic magnetoresistance (Chen et al. 2009).

In most cases, Fe–Co and Fe–Ni MNPs are synthesized having core–shell architecture. The core–shell design offers a possibility to control the product's physical and chemical properties in terms of the structure of the core, shell, and interface (Wang and Zeng 2009). Very frequently, the shell is of a metal oxide nature which, on one hand, protects the metals involved against oxidation, but, on the other hand, decreases, to some extent, the maximum material's magnetization that can be reached when exposing MNPs to external magnetic fields. In addition, it may provide functional groups for further functionalization to improve the biocompatibility of these MNPs with regard to their exploitation in biomedical areas. One of the main factors controlling the optimization of the morphological, structural, and magnetic properties of MNPs targeting particular applications is the synthesis route followed to obtain these (nano)materials. In the case of Fe–Co and Fe–Ni (nano)alloys, a rich variety of synthetic techniques have been reported so far, generally falling into two main groups, i.e., physical and chemical methods. They include hydrogen reduction of Fe, Co, and Ni inorganic salts (Suh et al. 2006; Otsuka et al. 1984), reverse micelles techniques (Suresh et al. 2011; Naik et al. 2011), hydrothermal reduction (Liu et al. 2010), sol–gel techniques (Shen et al. 2011; Xu et al. 2010), sonochemical decomposition (Li et al. 2003; Shafi et al. 1997), hydrogen plasma reaction (Dong et al. 1999; Li et al. 2001; Liu et al. 2010), inert gas condensation (Djekoun et al. 2009), etc. Each synthetic method, employed for preparation of a particular (nano)material, has advantages and drawbacks that unwind from its complexity regarding the use of precursors, conditions secured, steps involved, and time and cost demands. Among several preparative methods of magnetic nanostructures, the borohydride (ABH_4, A = Li, Na, K) reduction technique is widely adopted by synthetic chemists and materials scientists in terms of simplicity, safety, non-hazard, and versatility in both inorganic and organic chemistry. Most importantly, borohydride is an effective reducing agent of transition metal ions with its action being strongly influenced by the metal oxidation state, counterions, solvent, concentration, and temperature (Klabunde et al. 1994). Therefore, a library of new inorganic magnetic solids (metallic, ceramic, or composite) can be foreseen by the borohydride method via controlling one or more of the above-mentioned parameters (Bourlinos et al. 2004, 2005).

In this study, we describe the synthesis and characterization of highly magnetic core–shell MNPs of Fe–Co and Fe–Ni type, prepared by employing the borohydride reduction technique for the first time, and present a detailed study of their morphological,

structural, magnetic, and compositional properties. In particular, we utilize sodium borohydride as a reducing agent and suitable metal salts as a metal source, avoiding involvement of any organic solvent. Aqueous reduction results in phases having core–shell structure and consisting of a bimetallic Fe–Co and/or Fe–Ni alloy core and an iron oxyhydroxide shell of a ferrihydrite nature which can be easily modified for further functionalization. The highly biocompatible chemical composition of this oxyhydroxide phase in the shell empowers the potential of these MNPs for their possible exploitation in biomedical-related applications.

Experimental

Synthesis of materials

The two MNPs samples, hereafter denoted as the Fe–Ni and Fe–Co sample, were prepared by a wet chemical method using a sodium borohydride agent. In details, stoichiometric quantities of 526 mg of $NiSO_4{\cdot}6H_2O$, 784 mg of $(NH_4)_2Fe(SO_4)_2{\cdot}6H_2O$ and 562 mg of $CoSO_4{\cdot}4H_2O$, 784 mg of $(NH_4)_2Fe(SO_4)_2{\cdot}6H_2O$ (all supplied by Aldrich and used as-received), corresponding to $Fe_{50}Ni_{50}$ and $Fe_{50}Co_{50}$ stoichiometries, were completely dissolved in 100 ml glass beakers containing 20 ml of de-ionized water. 400 mg of $NaBH_4$ solid specimens (Aldrich, used as-received) were then rapidly added to each one of the two clear solutions under vigorous stirring. The mixtures were further allowed to stir under ambient conditions for 25 min. When the reactions were completed, the mixtures were transferred in clean 100 ml glass beakers. The magnetic solids were allowed to settle from the solution using a strong hand magnet, rinsed five times with 40 ml of de-ionized water and three times with 40 ml of acetone. The solids were finally dried in a hood at room temperature for 15–20 min, affording magnetic black powders.

Materials characterization

The resulting samples were characterized by powder X-ray diffraction (XRD) on a PANalytical X'Pert PRO diffractometer using Co K_α radiation, equipped with an X'Celerator detector. X-ray fluorescence (XRF) analysis was carried out by an XRF spectrometer (Wavelength dispersive XRF S4 Pioneer). Information on the morphology, stoichiometry, and particle size of the synthesized samples was extracted by transmission electron microscopy (TEM) using a JEM2010 microscope operated at 200 kV with a point-to-point resolution of 1.9 Å. Before measurements, the samples were dispersed in ethanol and the suspension was treated in ultrasound for 10 min. A drop of very dilute suspension was placed on a carbon-coated grid and allowed to dry by evaporation at ambient temperature. Magnetization measurements were performed employing a SQUID magnetometer (MPMS XL-7 type, Quantum Design). The hysteresis loops were collected at temperatures of 5 and 300 K in external magnetic fields ranging from −70 to +70 kOe. The zero-field-cooled (ZFC) and field-cooled (FC) magnetization curves were recorded on warming in the temperature range from 5 to 300 K under an external magnetic field of 100 Oe after cooling in a zero magnetic field and in a magnetic field of 100 Oe, respectively. The same measuring procedure was also applied for collecting the ZFC and FC magnetization curves in an external magnetic field of 1 kOe. ^{57}Fe Mössbauer spectra of the MNPs samples were collected in transmission geometry at 300, 77, and 5 K, using constant-acceleration spectrometers, equipped with ^{57}Co(Rh) sources kept at room temperature, liquid N_2 and liquid He bath Mössbauer cryostats (Oxford Instruments). Velocity calibration of the spectrometers was carried out using metallic α-iron at room temperature; all isomer shift values are given relative to this standard.

Results

Structural, compositional, size, and morphology characterization

XRD patterns of the two synthesized samples are shown in Fig. 1. In both patterns, we observe a very broad diffraction peak with a maximum at around 53° of 2θ. In addition, in the case of the Fe–Co sample, the two more broad diffraction peaks with maxima at around 40° and 71° of 2θ are evident, which are not detected in the XRD pattern of the Fe–Ni sample. The broadening of the diffraction peaks indicates the nanostructure nature of the studied samples. The main peak at 53° of 2θ suggests the presence of MNPs species with a body centered cubic (bcc) crystal

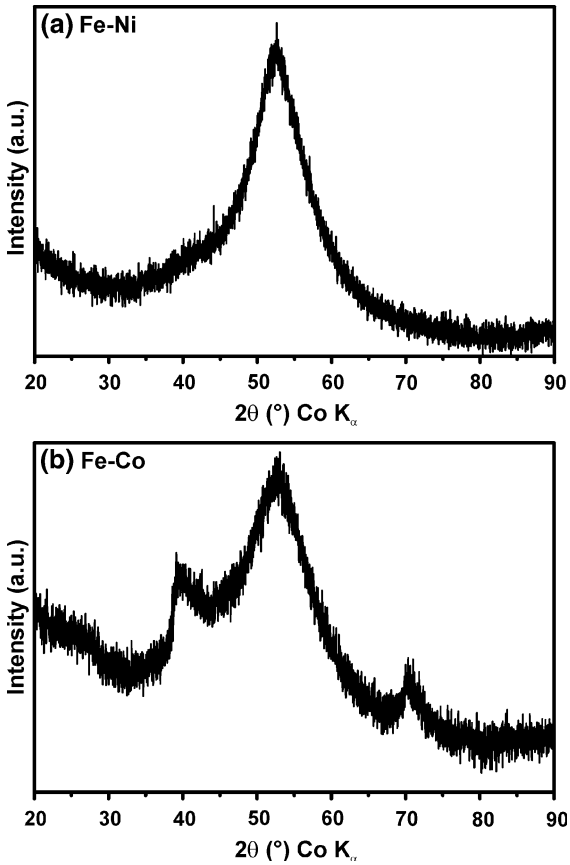

Fig. 1 XRD patterns of **a** Fe–Ni and **b** Fe–Co MNPs sample

structure, resembling that of α-Fe. The additional diffraction peaks observed for the Fe–Co sample are located in angular positions that are close to the broad reflections of the two-line ferrihydrite ($Fe_5HO_8{\cdot}4H_2O$) phase (Cornell and Schwertmann 1996). However, from the XRD pattern of the Fe–Ni sample, we cannot unambiguously exclude the presence of ferrihydrite phase; its diffraction peaks may be hidden in the background of the XRD signal due to its lower quantity in the Fe–Ni sample or ferrihydrate phase is more structurally amorphous in the Fe–Ni sample than in the Fe–Co sample.

Taking into account the total broadening of the main diffraction peak at 53° of 2θ and using the Scherrer formula (Cullity 1956), the average particle size is estimated to be below 2 nm for both samples, being a rather low value. However, the Scherrer formula gives only estimation of the size of the coherent particle domains and depends significantly on the broadening of the diffraction peak under investigation, in which other factors like the low degree of crystallinity of the prepared phases are also reflected. In such cases, the average particle size might be underestimated by this formula and far from a more accurate one derived from analysis of TEM images. Based on XRF measurements yielding relative atomic percentages, the average compositions of the two synthesized samples are quite close to the nominal ones, i.e., 52.6 % of Fe and 47.4 % of Ni for the Fe–Ni sample, and 46.4 % of Fe and 53.6 % of Co for the Fe–Co sample.

TEM images of the prepared Fe–Ni and Fe–Co samples are shown in Figs. 2 and 3, respectively. The images reveal that the samples have quite similar microstructure morphology and are composed of nanoparticles exhibiting a core–shell structure. Most particles have more or less spherical shapes, although some of them are more elongated than the others. The nanoparticles in both samples are also interconnected with each other as they seem to form assemblies of larger branch-type structures through attachment of their shells.

As it is further evident from TEM images, the prepared nanosystems exhibit a particle size distribution. The majority of the nanoparticles have their size values falling between 10 and 15 nm. For the larger nanoparticles, the shell volume seems to be much smaller than the core volume, whereas in the case of the smaller nanoparticles, the shell volume becomes comparable with the core volume. A more detailed statistically based analysis of several TEM images acquired for both samples gives the particle size distribution as depicted in Fig. 4. A log-normal type distribution, i.e.

$$N(x) = \frac{1}{xw\sqrt{2\pi}} e^{-\frac{(\ln x - \ln x_c)^2}{2w^2}}, \quad (1)$$

is best suited to fit the profile of size dispersions, where $N(x)$ is the number of nanoparticles with size x and w, x_c are fitting parameters. Fitting the experimental data with such distribution functions (i.e., solid lines in Fig. 4) gives a median particle size (x_c) of about 15 nm for both samples.

It is worth noting here that the shell thickness of the MNPs seems also to possess a size distribution. A detailed statistically based analysis (see Fig. 4c, d) suggests that these distributions are similar and also

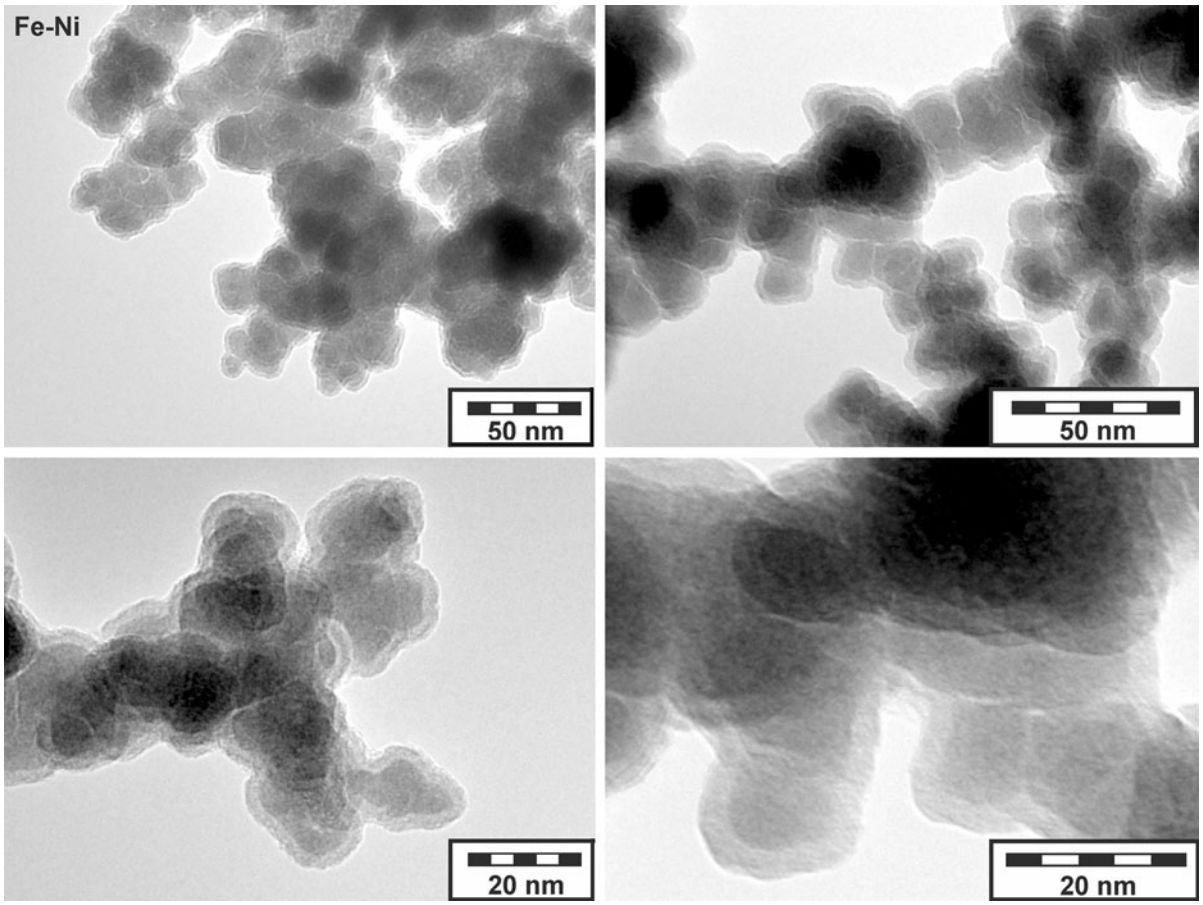

Fig. 2 TEM images of the synthesized Fe–Ni MNPs sample

resemble the profile of the particle size distributions of MNPs. Thus, the shell-size distribution is wider and extends more to the larger size values in the case of the Fe–Co sample compared to that of the Fe–Ni sample.

Magnetization measurements

Hysteresis loop measurements, carried out at temperatures of 5 and 300 K, are shown in Figs. 5 and 6. The measurements at 5 K were performed after cooling the samples under an applied magnetic field of 100 Oe. As it is evident, a complete saturation is not achieved in any of the studied samples, i.e., a non-zero dM/dH slope is observed in high applied magnetic fields at both measurement temperatures. In addition, this high field slope seems to show an increase for low-temperature hysteresis loop relative to the room temperature one in each sample, and, in particular, for the Fe–Co sample, this increase is more pronounced compared to that found for the Fe–Ni sample. For both samples, the hysteresis loops at 5 K display a small asymmetry in the absolute values of the positive and negative coercive fields (H_{C+} and H_{C-}), respectively (see insets in Figs. 5, 6 and Table 1). Due to core–shell architecture of the studied MNPs alloys, the maximum absolute magnetization values are quite lower than the saturation magnetization values of α-Fe at 300 K (218 emu/g) and 5 K (222 emu/g), or for $Fe_{50}Ni_{50}$ and $Fe_{50}Co_{50}$ bulk alloys, which generally possess even higher saturation magnetization values (Cullity and Graham 2009). This indicates that the nanoparticle shell is composed of a phase being magnetically weaker than that of nanoparticle core as frequently observed for such types of core–shell nanoparticles (Krishnan et al. 2006). The absolute values of the ($H_{C+} - |H_{C-}|$) difference at 5 K are significantly higher relative to the corresponding values at 300 K for

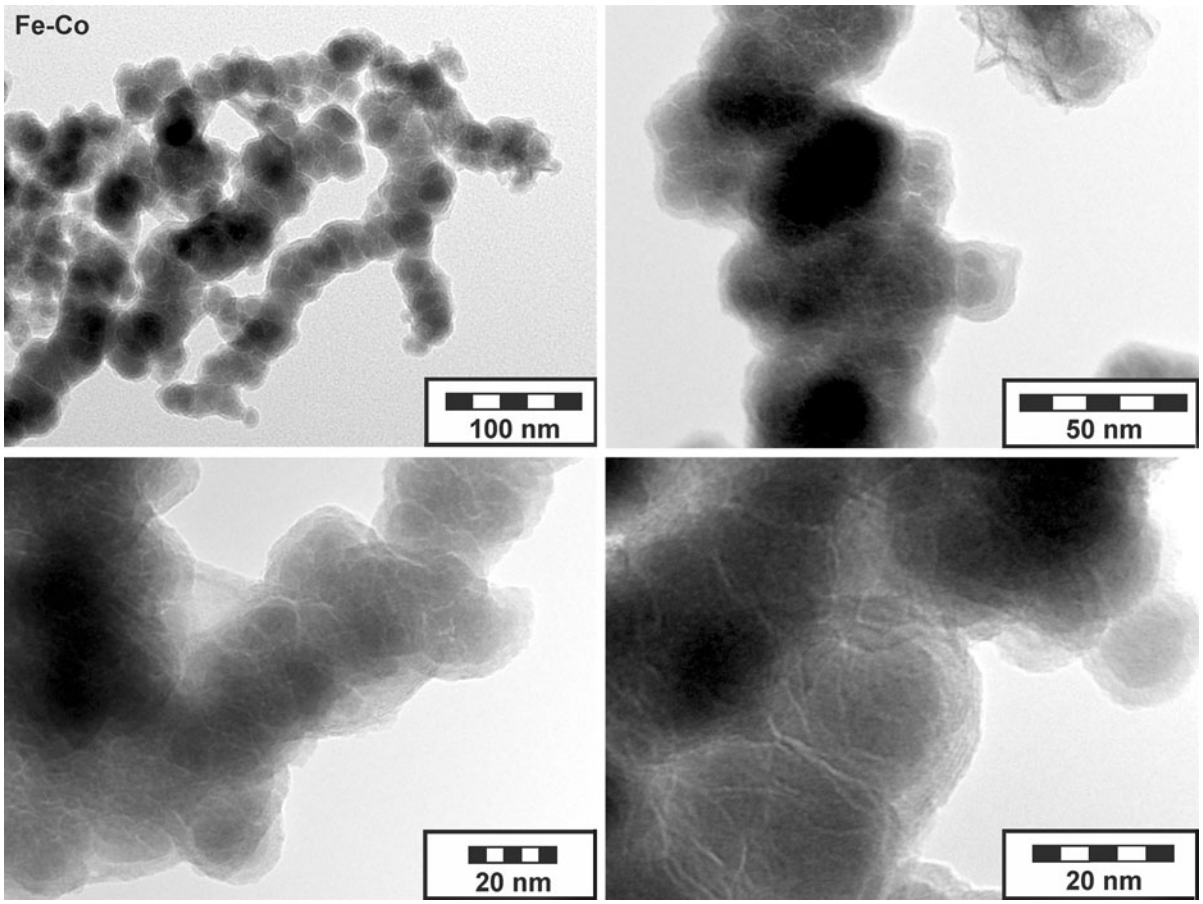

Fig. 3 TEM images of the synthesized Fe–Co MNPs sample

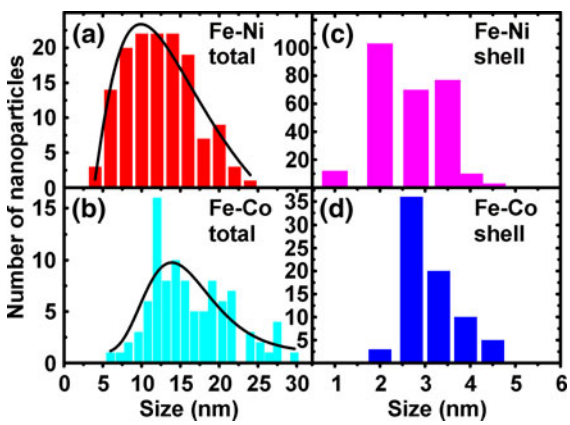

Fig. 4 **a** Particle size distribution, **b** particle size distribution, **c** shell thickness distribution of the synthesized Fe–Ni MNPs, and **d** shell thickness distribution of the synthesized Fe–Co MNPs as derived from TEM measurements. The *solid lines* in panels **a** and **c** are results of fitting procedure exploiting the log-normal distribution function

both studied samples. These characteristics reflect the nanostructured nature of the samples, and are expected in such MNPs systems (Fiorani 2005; Mørup and Hansen 2007; Gubin 2009). On the other hand, in such core–shell nanoparticle systems composed of phases with different magnetic properties, exchange-bias phenomenon is often observed. The above characteristics thus suggest the presence of a magnetic multi-phase system in the structure of our MNPs, implying the appearance of exchange-bias phenomenon in the interface between the phases exhibiting different magnetic orderings. However, at 300 K, the hysteresis loops are more symmetric and the absolute $(H_{C+} - |H_{C-}|)$ difference is close to zero, indicating a decrease in the strength of this phenomenon, which seems to vanish.

In order to investigate further the nature and strength of this exchange-bias phenomenon occurring in our samples, we performed additional hysteresis

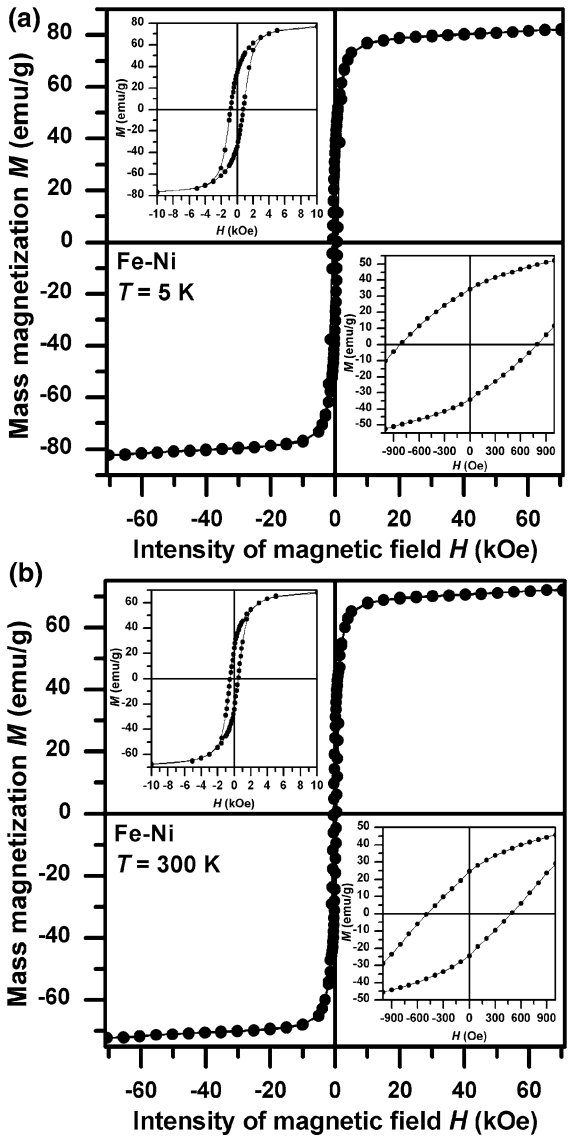

Fig. 5 Hysteresis loops of the synthesized Fe–Ni MNPs, recorded at a temperature of **a** 5 and **b** 300 K. The *insets* show the profile of the hysteresis loop around the origin

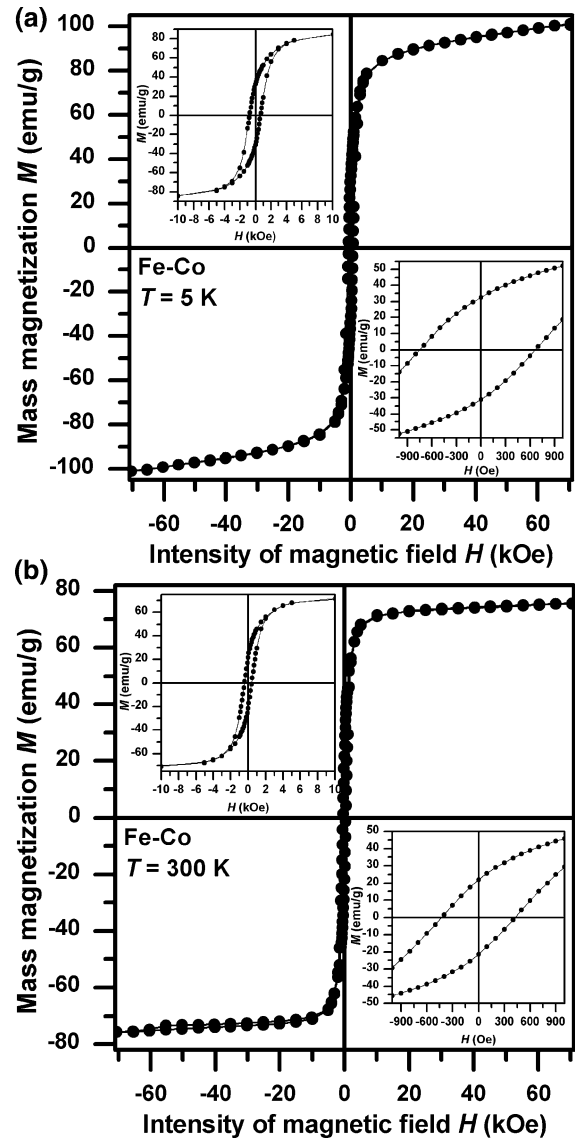

Fig. 6 Hysteresis loops of the synthesized Fe–Co MNPs, recorded at a temperature of **a** 5 and **b** 300 K. The *insets* show the profile of the hysteresis loop around the origin

loop measurements at 5 K, after cooling the samples from 300 K under an applied magnetic field of +70 kOe. The resulting loops are shown in Fig. 7 and their features are listed in Table 1. These measurements do not differ much from the measurements performed in a quite smaller cooling magnetic field of 100 Oe. This indicates that the exchange-bias effect between different magnetically ordered phases is rather weak, most probably due to a low value of the magnetic anisotropy of some of the phases involved in these interactions.

The temperature evolution of magnetization also confirms the nanostructured nature of both investigated samples. ZFC and FC magnetization curves, recorded under applied magnetic fields of 100 and 1 kOe for the synthesized Fe–Ni and Fe–Co MNPs samples, are shown in Figs. 8 and 9. On increasing the temperature, ZFC magnetization curves of both samples show an abrupt increase in the magnetization values up to 25 K, followed by a more gradual and constant increase at higher temperatures. This is in contradiction with the typical magnetic response

Table 1 Parameters of the hysteresis loops of the Fe–Ni and Fe–Co samples, measured at temperatures of 5 and 300 K, where M_{max+} and M_{max-} are the maximum magnetizations at +70 and −70 kOe, H_{C+} and H_{C-} are the positive and negative coercivities, and M_{R+} and M_{R-} are the positive and negative remanent magnetizations, respectively

Sample	T (K)	M_{max+} (emu/g)	M_{max-} (emu/g)	H_{C+} (Oe)	H_{C-} (Oe)	$H_{C+} - \lvert H_{C-} \rvert$ (Oe)	M_{R+} (emu/g)	M_{R-} (emu/g)
Fe–Ni	5	82.25	−82.25	798	−821	−23	34.48	−34.27
	300	72.19	−72.19	489	−490	−1	24.44	−24.42
Fe–Co	5	101.01	−101.01	667	−751	−84	32.67	−31.05
	300	75.66	−75.66	425	−426	−1	21.75	−21.68
Fe–Ni*	5	84.68	−84.68	778	−796	−18	36.12	−35.33
Fe–Co*	5	100.17	−100.17	682	−736	−54	32.14	−30.53

Typical errors are ±0.01 emu/g for the magnetization values and ±5 Oe for the coercive field values. The lines indicated with * refer to the hysteresis loops measured after cooling down to 5 K under an applied magnetic field of +70 kOe

exhibited by superparamagnetic nanoparticle systems (Fiorani 2005; Mørup and Hansen 2007), which implies that MNPs in the studied samples do not show a superparamagnetic behavior in the whole nanoparticle volume, probably as a result of possible multidomain structure and exchange interactions taking place between the nanoparticle core and shell.

However, there is a difference in the nature of the steep increase in the magnetization values of the studied samples below 25 K as witnessed from the ZFC magnetization curves. For the Fe–Ni sample, this increase extends from 5 to 15 K in both applied magnetic fields. In the case of the Fe–Co sample, under 100 Oe, magnetization values are stable from 5 to 10 K and an increase is observed from 10 to 20 K, whereas under 1 kOe, the increase in magnetization values is constant from 5 to 20 K.

FC magnetization curves follow an almost linear increase down to 5 K in the case of the Fe–Ni sample under both applied magnetic fields. In the case of the Fe–Co sample, the corresponding increase is lower than that observed for the Fe–Ni sample within a large temperature region, and a steeper increase in the magnetization values is observed under both applied magnetic fields below 20 K, which is absent in the corresponding curves of the Fe–Ni sample. ZFC and FC magnetization curves do not coincide at any temperature region and seem to bifurcate at a temperature higher than 300 K.

Mössbauer spectroscopy measurements

Mössbauer spectra of the prepared samples, collected at 5, 77, and 300 K, are shown in Fig. 10. The spectral characteristics, derived for the two samples at each recorded temperature, are very similar. At 77 and 300 K, the acquired Mössbauer spectra for both investigated samples are quite broad, but at 5 K, they seem to be significantly more resolved. At 77 and 300 K, a quadrupole split contribution is evident at the center of each spectrum, while a magnetically split part with asymmetrically broaden absorption lines occupies the majority of the absorption area. In order to fit the Mössbauer spectra at 77 and 300 K adequately, we used a set of one quadrupole split (P) and one magnetically split (M) component. For M component, we allowed an asymmetric spreading (ΔB_{hf}, Gaussian type) of the hyperfine magnetic field (B_{hf}) values around a central value (B_{hf}^{C}) in order to describe the asymmetric broadening (Douvalis et al. 2010). The resulting Mössbauer hyperfine parameters are listed in Table 2. The isomer shift (δ) values of P component lie in the characteristic range for high-spin ($S = 5/2$) Fe^{3+} in oxygen environment, while the δ values of P component refer to iron atoms close to a metallic state for both samples (Greenwood and Gibb 1971).

The P and M spectral components are no longer present in the 5 K Mössbauer spectrum of both studied samples as magnetically split contributions with narrow absorption lines dominate their spectral profile. It is evident that three main sextets are needed to fit these spectra. However, the central part of the spectrum still possesses some broadening, which suggests the presence of an additional minor broad magnetically split contribution. The resulting δ values for the two main components (M1 and M2) are quite lower than the corresponding values of the third and fourth components (M3 and M4). These values, together with the quadrupole shift (ΔE_Q) values,

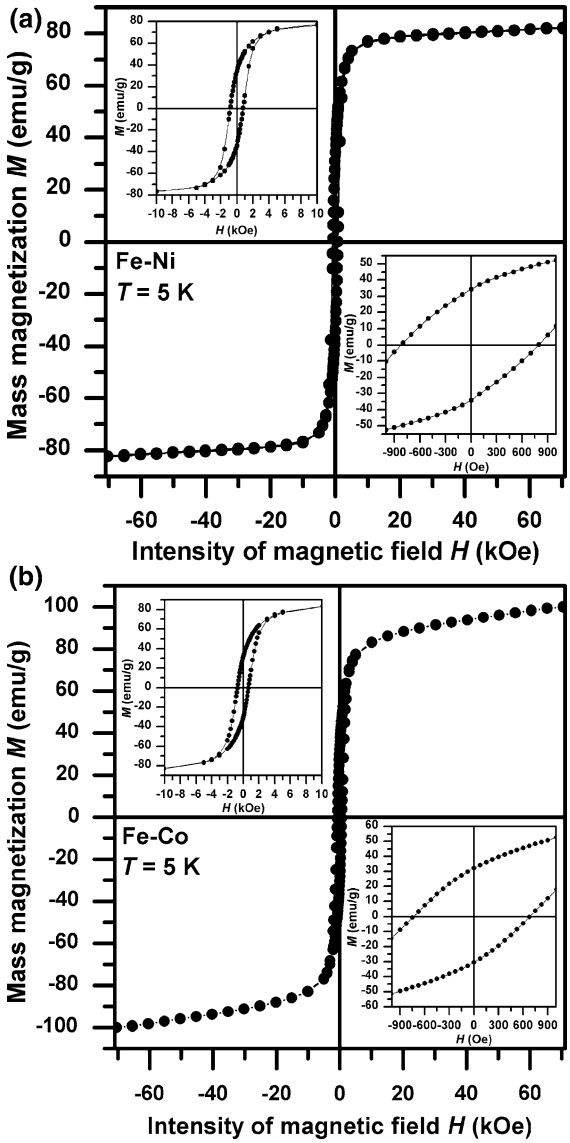

Fig. 7 Hysteresis loop of **a** Fe–Ni and **b** Fe–Co MNPs, recorded at a temperature of 5 K after cooling from 300 K under an applied magnetic field of +70 kOe. The *insets* show the profile of the hysteresis loop around the origin

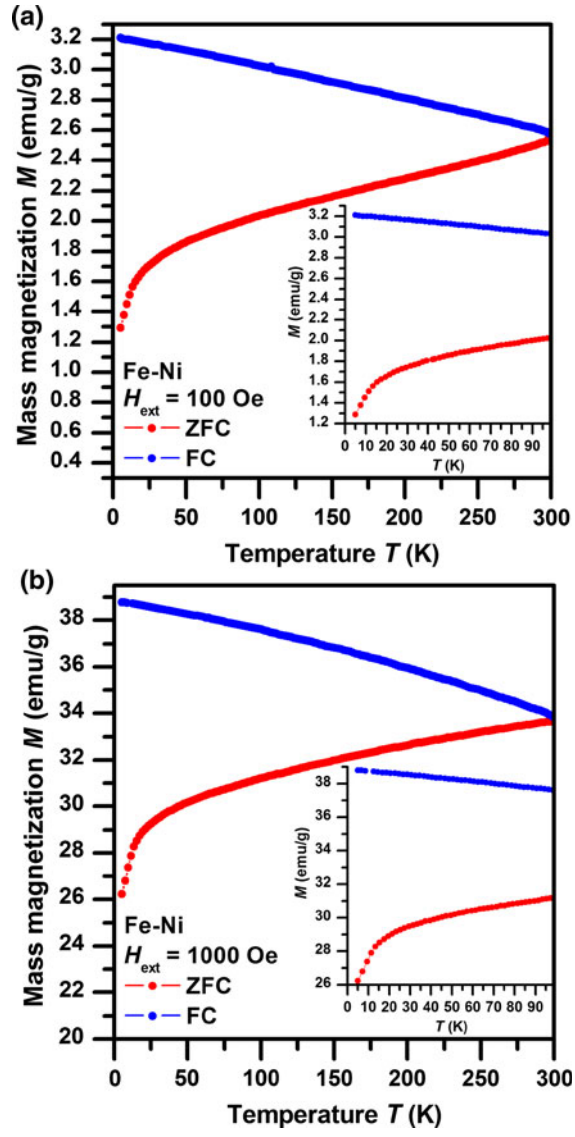

Fig. 8 ZFC and FC magnetization curves of the synthesized Fe–Ni MNPs, recorded under an applied magnetic field of **a** 100 Oe and **b** 1 kOe. The *insets* show the profiles of the ZFC and FC magnetization curves at low temperatures

derived for M1 and M2 component, correspond to Fe atoms of "metallic" character whereas those of M3 and M4 component are typical of high-spin Fe^{3+} ions. To be more specific, M1 component in both spectra displays hyperfine parameter values that are close to those of bcc metallic α-iron (Greenwood and Gibb 1971), while M2 component shows a somewhat higher δ and ΔE_Q values and lower B_{hf}^C value as compared with those derived for M1 component. The δ values of M3 and M4 components are quite close to each other in each spectrum, but their B_{hf}^C and ΔB_{hf} values are quite different. M3 component shows a larger B_{hf} and smaller ΔB_{hf} values, respectively, than those derived for M4 component. These results suggest that these two components might be closely related (i.e., identical Fe^{3+} oxidation states), however, they reflect different magnetic characteristics, probably as a result of finite-size effects. For both samples, the sum of the

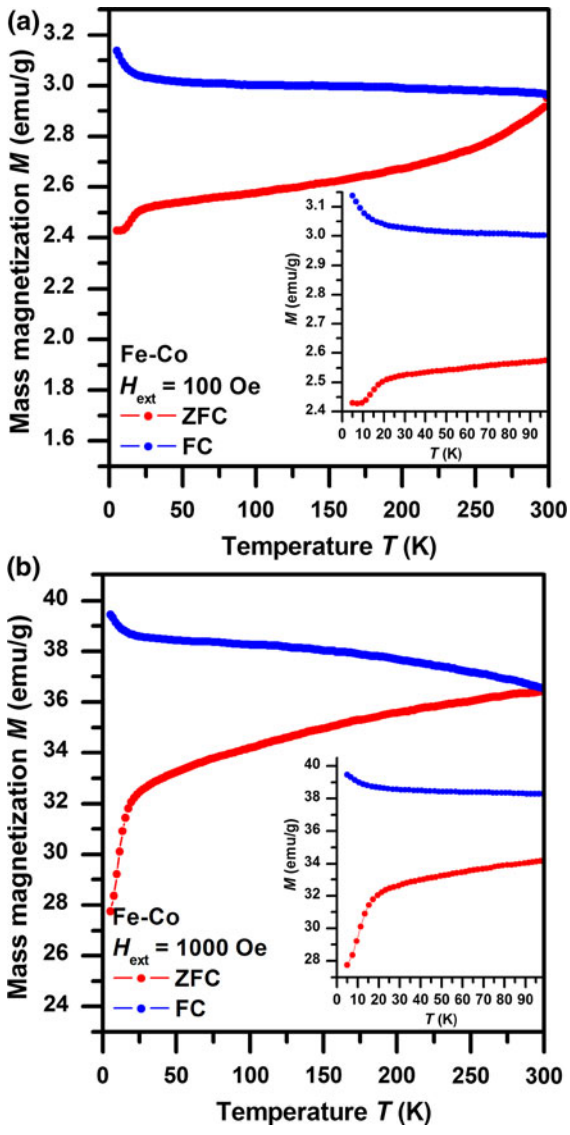

Fig. 9 ZFC and FC magnetization curves of the synthesized Fe–Co MNPs, recorded under an applied magnetic field of **a** 100 Oe and **b** 1 kOe. The *insets* show the profiles of the ZFC and FC magnetization curves at low temperatures

absorption area of the Fe^{3+} M3 and M4 component at 5 K lies, within the experimental error of the Mössbauer technique, in the range of the absorption area value of P component used to fit 77 and 300 K Mössbauer spectra. Similarly, the absorption area of the "metallic" M1 and M2 component at 5 K sums up to almost the same value of the absorption area found for M component at 77 and 300 K. The corresponding δ values of P and M3, M4 component also follow the expected variation, with respect to temperature, due to the second-order Doppler shift effect (Greenwood and Gibb 1971). The δ values of M component follow a similar variation from 300 to 77 K, and at 5 K, the δ values of M1 and M2 components are found in the same range as the δ value of M component at 77 K. Thus, there is a strong evidence of direct correspondence of P component to M3 and M4 component, and of M component to M1 and M2 component.

Discussion

The presented results confirm that the Fe–Ni and Fe–Co samples are both composed of nanoparticle assemblies with core–shell architecture. While the nanoparticle core is magnetically ordered in the temperature interval of 5–300 K, the nanoparticle shell exhibits a transition to a superparamagnetic regime on increasing the temperature. The relatively large room temperature coercive fields indicate a ferromagnetically ordered state of the nanoparticle core at 300 K due to a possible multi(magnetic)-domain structure in the nanoparticle core and/or presence of strong interparticle interactions of both dipole–dipole and exchange nature. Coercivity and remanence values can be generally enhanced on emergence of finite-size effects as MNPs approach a size when a magnetic multi-domain state collapses into single-domain regime (Cullity and Graham 2009). For $Fe_{50}Co_{50}$ and $Fe_{50}Ni_{50}$ noninteracting spherical nanoparticles, the critical size at which the transition from multi-domain regime to single-domain state occurs is estimated to be $\sim$8.5 and $\sim$12 nm, respectively (Majetich and Jin 1999; Bertotti 1998). In addition to the effect of oxyhydroxide shell weakening the magnetic response of MNPs, the reduced maximum magnetization values and non-saturation profile of the hysteresis loops in high applied magnetic fields (especially at 5 K) suggest the existence of a variety of magnetic coupling interactions of ferromagnetic and antiferromagnetic origin, having been developed in the structure of these MNPs. These features can be attributed to the presence of different magnetically ordered phases, due to their core–shell structure, which might introduce exchange-bias effects. The firm magnetic coupling between the Fe–Co or Fe–Ni core and oxyhydroxide shell then shifts the blocking temperature of Fe–Co and Fe–Ni nanoparticle cores to temperatures higher than 300 K as already reported

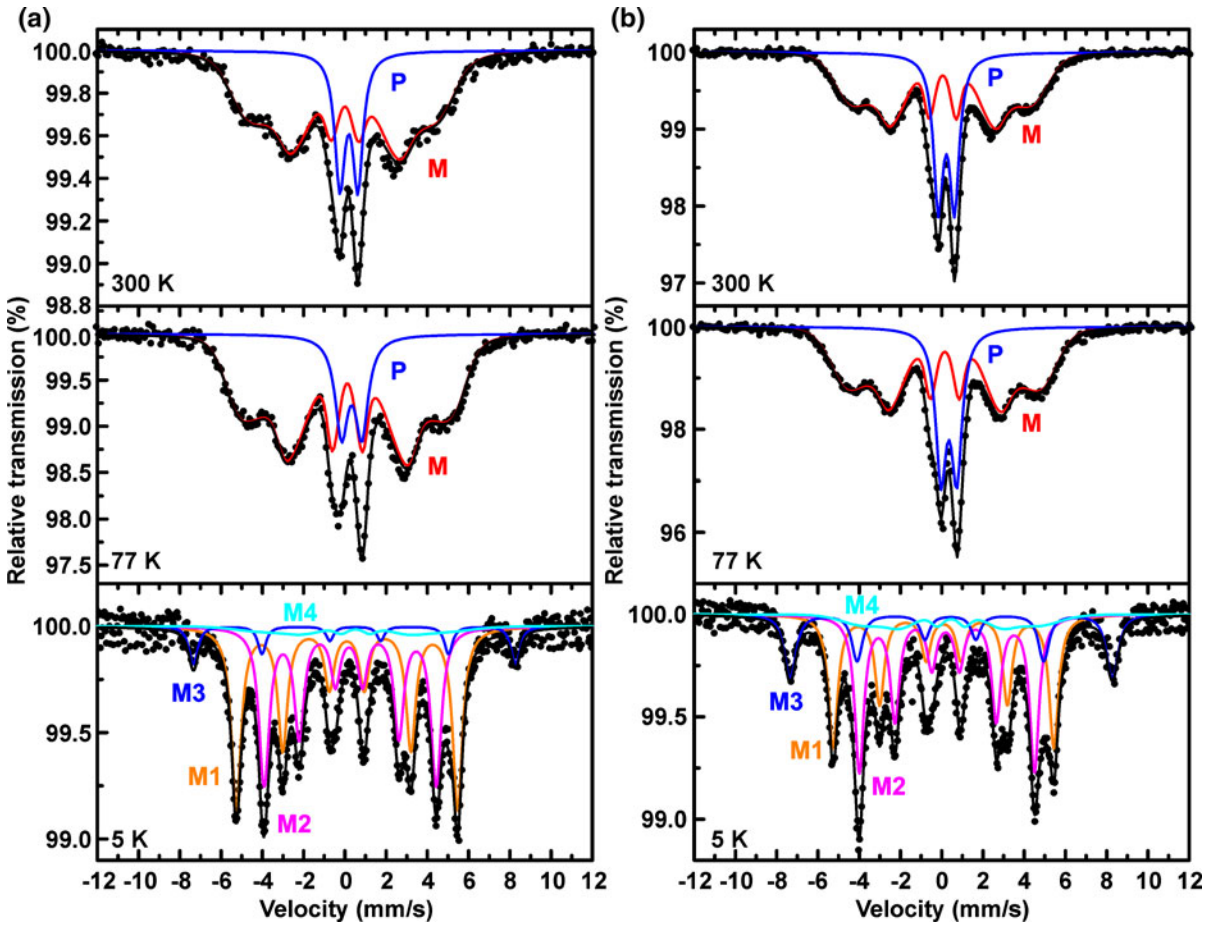

Fig. 10 ^{57}Fe Mössbauer spectra of **a** Fe–Ni and **b** Fe–Co MNPs sample recorded at various temperatures

for other systems of nanoparticles with core–shell architecture when the ferromagnetic nanoparticle core is magnetically coupled with the nanoparticle shell exhibiting magnetic ordering distinct from that of the core (Nogues et al. 2005). This may explain why a room temperature superparamagnetic behavior is not observed in the synthesized Fe–Co and Fe–Ni samples although the size of the nanoparticles in the studied systems is below the superparamagnetic limit ($\sim$34 and $\sim$71 nm for $Fe_{50}Co_{50}$ and $Fe_{50}Ni_{50}$, respectively) (Majetich and Jin 1999; Mazaleyrat et al. 2009).

However, some differences in magnetization characteristics of the Fe–Co and Fe–Ni samples unfold important information on their magnetic properties: (i) The absolute average H_C values of the Fe–Ni sample are greater than those of the Fe–Co sample both at 5 and 300 K. This mainly reflects the nature of the different magnetic properties of the alloys as Fe–Co is expected to be magnetically softer than Fe–Ni (Cullity and Graham 2009). (ii) The absolute ($H_{C+} - |H_{C-}|$) difference at 5 K is higher for the Fe–Co sample, suggesting a stronger exchange-bias coupling between different magnetically ordered phases compared to that occurring in the Fe–Ni sample.

Moreover, a steeper increase in the magnetization values, observed in the FC magnetization curve of the Fe–Co sample at low temperatures, demonstrates the presence of a multi-phase magnetic system. This steep increase cannot be attributed to the exchange-bias effect as this phenomenon tends to suppress the total magnetization values. It seems that another component of the MNPs system comes into play at low temperatures. This component should be of superparamagnetic nature and enters a magnetically ordered regime below a blocking temperature at 20–25 K,

Table 2 Mössbauer hyperfine parameters of the Fe–Ni and Fe–Co MNPs samples, derived from the Mössbauer spectra measured at 300, 77, and 5 K

Sample	T (K)	δ (mm/s)	$\Gamma/2$ (mm/s)	ΔE_Q (mm/s)	B_{hf}^C (kOe)	ΔB_{hf}^L $B_{hf} < B_{hf}^C$ (kOe)	ΔB_{hf}^R $B_{hf} > B_{hf}^C$ (kOe)	A (%)	Component	Assignment
Fe–Ni	300	0.05	0.34	−0.12	284	48	23	80	M	Metallic Fe–Ni in core
		0.30	0.30	0.87	–	–	–	20	P	Fe^{3+} in shell
	77	0.19	0.24	−0.08	317	53	19	84	M	Metallic Fe–Ni in core
		0.44	0.38	0.98	–	–	–	16	P	Fe^{3+} in shell
	5	0.10	0.28	0.01	333	0	0	45	M1	Fe "rich" phase in core
		0.23	0.28	0.05	259	3	3	41	M2	Fe "poor" phase in core
		0.48	0.21	−0.04	485	3	3	8	M3	Fe^{3+} in shell
		0.49	0.25	−0.06	268	39	39	6	M4	Fe^{3+} in shell
Fe–Co	300	0.13	0.21	−0.06	271	38	23	70	M	Metallic Fe–Co in core
		0.33	0.28	0.78	–	–	–	30	P	Fe^{3+} in shell
	77	0.24	0.24	−0.04	291	38	22	72	M	Metallic Fe–Co in core
		0.46	0.31	0.77	–	–	–	28	P	Fe^{3+} in shell
	5	0.09	0.27	0.00	332	0	0	33	M1	Fe "rich" phase in core
		0.22	0.27	0.06	264	0	0	39	M2	Fe "poor' phase in core
		0.44	0.27	0.04	485	4	4	19	M3	Fe^{3+} in shell
		0.46	0.26	0.01	261	29	29	9	M4	Fe^{3+} in shell

δ is the isomer shift (relative to α-Fe at 300 K), Γ is the half linewidth, ΔE_Q is the quadrupole splitting, B_{hf}^C is the central value of the hyperfine magnetic field, ΔB_{hf}^L and ΔB_{hf}^H are the asymmetric spreadings of B_{hf}^C (see text), and A is the relative spectral absorption area of each component. Typical errors are ± 0.02 mm/s for δ, Γ, and ΔE_Q, ± 3 kOe for B_{hf}^C and ± 5 % for A

giving consequently rise to higher magnetization values. As these features are observed only for the Fe–Co sample, it implies that in the Fe–Ni sample, this superparamagnetic phase acquires different magnetic characteristics, most probably due to a larger local magnetic anisotropy that Co atoms possess relative to Ni atoms and different degree of shell crystallinity of Fe–Ni MNPs compared to that of shell crystallinity of Fe–Co MNPs (as proved by XRD analysis).

A deeper insight into magnetic structure of the studied samples can be drawn from the analysis of the measured Mössbauer spectra, taking into account knowledge on structural properties and stoichiometry available from XRD and XRF measurements. In particular, XRD results show the presence of a metallic bcc nanostructured phase in both samples. We can assign M1 component to Fe atoms with their local environment comprised, to a large extent, of other Fe atoms alone as their hyperfine parameters are not affected much by the presence of neighboring Ni or Co atoms in the crystal structure. We can call this phase as an "iron-rich" phase. On the other side, the shifted values of hyperfine parameters of M2 component, relative to those of M1 component (see Table 2), reflect the presence of increased number of Ni or Co atoms in the near environment of the probed Fe atoms in both samples. These values correspond well with those found for Fe–Ni and Fe–Co alloys in the iron "poorer" regions (Johnson et al. 1961, 1963; Wertheim et al. 1964). Thus, we can assign M2 component to an existence of "iron-poor" phase in MNPs.

The remaining components (M3 and M4) used to fit the 5 K spectra reflect iron oxyhydroxide phases. In particular, M3 component, which is more magnetically resolved at 5 K, displays hyperfine parameter values that are quite close to two-line ferrihydrite (Cornell and Schwertmann 1996). We can suggest that M3 and M4 components represent the shell of MNPs, which is composed of poorly crystallized to amorphous ferrihydrite. The reason to use two (M3 and M4) components instead of one (M3) component for this phase can be justified adopting following aspects. First, the absorption area of M3 component lacks a significant amount of the corresponding value found for the related Fe^{3+}

P component, and M4 component fulfills, within the experimental errors, this gap. Second, if the shell of MNPs corresponds, as suggested, to an oxyhydroxide layer, some of the nanoparticles (as seen in TEM images) possess a quite thin shell layers. Thus, small thickness, and consequently mass, will probably deprive Fe^{3+} ions, located in these shells, from developing a complete magnetic hyperfine splitting, leaving them in an intermediate, but not complete superparamagnetic state even at temperatures as low as 5 K. In addition, the oxyhydroxide shells may probably contain not only Fe^{3+} ions, but Ni^{2+} or Co^{2+} ions as well, and the presence of these ions in the structure of the shell phase may also influence local electronic and magnetic properties. For these reasons, M4 component is attributed to the nanoparticle shells that, although they exhibit in average the same local chemical characteristics as those derived from M3 component, they behave in a different magnetic manner, showing a more significant superparamagnetic phenomenon (i.e., faster superparamagnetic relaxation) (Mørup and Hansen 2007).

By assigning M3 and M4 components to the shell of MNPs, "metallic" M1 and M2 components are left to account for the nanoparticle core. However, comparable values of spectral areas of M1 and M2 components indicate a significant number of Fe atoms being involved in the interaction with Ni or Co atoms as almost half (41 % out of 86 % in the case of the Fe–Ni sample) or more than half (39 % out of 72 % in the case of the Fe–Co sample) of metallic Fe atoms in total, present in each sample, are engaged within this interaction mechanism. In other words, this points to a compositional variation, at the atomic level, in the core of our MNPs. Such compositional variation between the alloy nanoparticles in the present bimetallic systems is expected on account of the different reduction potentials of the combined metals, i.e., one metal tends to precipitate faster than the other one as a result of easier chemical reduction by borohydride.

Moreover, the relative spectral absorption areas of each component at 5 K reveal important information on a relative population of each phase in the studied samples. Thus, if similar Debye–Waller factors (Greenwood and Gibb 1971) are assigned to each component in both samples, by comparing the relative spectral area values of M1 components in the two 5 K spectra, it is evident that the number of Fe atoms in the "iron-rich" phase of Fe–Ni MNPs seems to be higher than that of Fe atoms in the "iron-rich" phase of Fe–Co MNPs. However, comparing the absorption areas of M2 components, the relative populations of the "iron-poor" phase in the two samples seem to be quite similar. On the other side, for the Fe–Ni sample, the sum of the relative spectral areas of M3 and M4 components is quite lower than that found in the case of the Fe–Co sample, showing thus the opposite relation to the behavior of the "iron-rich" M1 component. This gives a proof that the spectral areas of these components, and their related P and M components, are interconnected, in the sense that an increase in the oxyhydroxide shell is related to the decrease in the "iron-rich" phase. Thus, Fe–Co MNPs have relative thicker oxyhydroxide shells than those of Fe–Ni MNPs. XRD, TEM, and magnetization measurements support this suggestion and indicate that the shell of Fe–Co MNPs is also relatively better crystallized than that of Fe–Ni MNPs.

It is known that ferrihydrite gradually develops magnetic ordering through a broad magnetic transition temperature region (130–70 K) (Cornell and Schwertmann 1996), and a complete magnetic ordering is established within a relatively broad temperature interval from 45 to 10 K or even at lower temperatures; the nature of this magnetic ordering depends on formation-preparation conditions and presence of other non-Fe^{3+} ions. Its low-temperature magnetic structure has been described to take variable forms, i.e., from ferrimagnetic (due to random spin arrangement) to speromagnetic or amorphous magnetic one (Pankhurst and Pollard 1992; Madsen and Mørup 1986). This then explains a weak exchange bias observed in the studied samples as the ferrihydrite shell, the magnetic properties of which may vary, does not acquire a strong magnetic anisotropy.

However, the magnetization measurements suggest that the shells of Fe–Co MNPs are more magnetically "active" than those of Fe–Ni MNPs. In other words, apart from being less well-crystallized, the shell phase of Fe–Ni MNPs sample gives much weaker contribution to the overall low-temperature (<25 K) MNPs magnetic response compared to that of the shell phase of Fe–Co MNPs as a result of its quantity, composition, and magnetic properties. This implies that the

shell phase of Fe–Ni MNPs is not only structurally amorphous, but also magnetically amorphous.

Conclusions

In this study, we reported the synthesis of the highly magnetic Fe–Co and Fe–Ni MNPs alloys exploiting a sodium borohydride agent without a need of any organic solvent. As a result, spherically shaped nanoparticles with a relatively narrow size distribution and core–shell structure were synthesized, having a combination of very interesting structural and magnetic properties. The acquired data show that the nanoparticle core is composed of metallic Fe–Ni or Fe–Co alloys, which are inhomogeneous at the atomic level, as both Fe "rich" and Fe "poor" alloy phases are detected. The shell is composed of a semi-amorphous-to-completely amorphous oxyhydroxide layer, close to the ferrihydrite composition. The core experiences a superparamagnetic relaxation due to its reduced size in each nanoparticle, which, however, does not lead to a complete superparamagnetic collapse of the corresponding ^{57}Fe B_{hf} values in alloys up to 300 K. On the contrary, the shell, due to its reduced mass and different magnetic properties, experiences a fast superparamagnetic relaxation, which leads to a complete collapse of the ^{57}Fe B_{hf} values in the oxyhydroxide at temperatures above $\sim$25 K. Weak exchange-bias effects are observed in the interface between the core and shell phases, and their reduced strength, as compared to that observed in other core–shell MNPs systems (Skumryev et al. 2003), is attributed to the superparamagnetic nature and low magnetic anisotropy of the shell phase.

Ferrihydrite is known to be a fully biocompatible material (Wu et al. 2008; Pardoe et al. 2003; Webb et al. 1999) as it is claimed to compose the inorganic core of ferritin, an important iron-storage molecule (Ford et al. 1984). Thus, the shell nature of the prepared MNPs provides them with enhanced biocompatibility for their possible use in biomedical-related applications. Beside this, it forms a barrier for further oxidation or erosion of the metallic core, avoiding thus degradation of its magnetic properties. In addition, the ability of chemical modification of this shell with substitution or addition of other ions or molecules might equip these MNPs with a variety of active functions, which, together with their intrinsic magnetic properties, may lead to development of novel versatile materials for many technological applications.

Acknowledgments The authors gratefully acknowledge the support by the Operational Program Research and Development for Innovations—European Regional Development Fund (Project No. CZ.1.05/2.1.00/03.0058) of the Ministry of Education, Youth, and Sports of the Czech Republic and by the Academy of Sciences of the Czech Republic (Project No. KAN115600801).

References

Berry CC, Curtis ASG (2003) Functionalisation of magnetic nanoparticles for applications in biomedicine. J Phys D 36:R198–R206. doi:10.1088/0022-3727/36/13/203

Bertotti G (1998) Hysteresis in magnetism. Academic Press, San Diego

Bourlinos AB, Panagiotopoulos I, Niarchos D, Petridis D (2004) Hydrophilic Co–Pt alloy nanoparticles: synthesis, characterization, and perspectives. J Mater Res 19:1227–1233. doi:10.1557/JMR.2004.0159

Bourlinos AB, Bakandritsos A, Petridis D (2005) One-pot borohydride synthesis of magnetically modified lepidocrocite. Chem Lett 34:666–667. doi:10.1246/cl.2005.666

Chen YZ, Luo XH, Yue GH, Luo XT, Peng DL (2009) Synthesis of iron–nickel nanoparticles via a nonaqueous organometallic route. Mater Chem Phys 113:412–416. doi:10.1016/j.matchemphys.2008.07.118

Chu SY, Kline C, Huang MQ, MacHenry ME, Cross J, Harris VG (1999) Preparation, characterization and magnetic properties of an ordered FeCo single crystal. J Appl Phys 85:6031–6033. doi:10.1063/1.369072

Cornell RM, Schwertmann U (1996) The iron oxides: structure, properties, reactions, occurrences and uses. Wiley-VCH, Weinheim

Cullity BD (1956) Elements of X-ray diffraction. Addison-Wesley, Massachusetts

Cullity BD, Graham CD (2009) Introduction to magnetic materials. Wiley, New Jersey

Djekoun A, Boudinar N, Chebli A, Otmani A, Benabdeslem M, Bouzabata B, Greneche JM (2009) Characterization of Fe and $Fe_{50}Ni_{50}$ ultrafine nanoparticles synthesized by inert gas-condensation method. Physica B 404:3824–3829. doi:10.1016/j.physb.2009.07.074

Dong XL, Zhang ZD, Zhao XG, Chuang YC, Jin SR, Sun WM (1999) The preparation and characterization of ultrafine Fe–Ni particles. J Mater Res 14:398–406. doi:10.1557/JMR.1999.0058

Douvalis AP, Polymeros A, Bakas T (2010) IMSG09: a ^{57}Fe–^{119}Sn Mossbauer spectra computer fitting program with novel interactive user interface. J Phys: Conf Ser 217:012014. doi:10.1088/1742-6596/217/1/012014

Fiorani D (2005) Surface effects in magnetic nanoparticles. Springer, New York

Ford GC, Harrison PM, Rice DW, Smith JM, Treffry A, White JL, Yariv J (1984) Ferritin: design and formation of an

iron-storage molecule. Philos Trans R Soc B 304:551–565. doi:10.1098/rstb.1984.0046

Greenwood NN, Gibb TC (1971) Mössbauer spectroscopy. Chapman and Hall Ltd., London

Gubin SP (2009) Magnetic nanoparticles. Wiley-VCH, Weinheim

Habib AH, Ondeck CL, Chaudhary P, Bockstaller MR, McHenry ME (2008) Evaluation of iron–cobalt/ferrite core–shell nanoparticles for cancer thermotherapy. J Appl Phys 103:07A307. doi:10.1063/1.2830975

He H, Heist RH, McIntyre BL, Blanton TN (1997) Ultrafine nickel particles generated by laser-induced gas phase photonucleation. Nanostruct Mater 8:879–888. doi:10.1016/S0965-9773(98)00016-6

Hoinville J, Bewick A, Gleeson D, Jones R, Kasyutich O, Mayes E, Nartowski A, Warne B, Wiggins J, Wong K (2003) High density magnetic recording on protein-derived nanoparticles. J Appl Phys 93:7187–7189. doi:10.1063/1.1555896

Jang HD, Hwang DW, Kim DP, Kim HC, Lee BY, Jeong IB (2004) Preparation of cobalt nanoparticles by hydrogen reduction of cobalt chloride in the gas phase. Mater Res Bull 39:63–70. doi:10.1016/j.materresbull.2003.09.023

Johnson CE, Ridout MS, Cranshaw TE, Madsen PE (1961) Hyperfine field and atomic moment of iron in ferromagnetic alloys. Phys Rev Lett 6:450–451. doi:10.1103/PhysRevLett.6.450

Johnson CE, Ridout MS, Cranshaw TE (1963) The Mössbauer effect in iron alloys. Proc Phys Soc 81:1079–1090. doi:10.1088/0370-1328/81/6/313

Kim SS, Kim ST, Ahn JM, Kim KH (2004) Magnetic and microwave absorbing properties of Co–Fe thin films plated on hollow ceramic microspheres of low density. J Magn Magn Mater 271:39–45. doi:10.1016/j.jmmm.2003.09.012

Klabunde KL, Stark JV, Koper O, Mohs C, Khaleel A, Glavee G, Zhang D, Sorensen CM, Hadjipanayis GC (1994) Chemical synthesis of nanophase materials. In: Hadjipanayis GC, Siegel RW (eds) Nanophase materials: synthesis–properties–applications. NATO Advanced Science Institutes Series, Series E, Applied Science, vol 260. Kluwer, Dordrecht, pp 1–19

Kodama RH (1999) Magnetic nanoparticles. J Magn Magn Mater 200:359–372. doi:10.1016/S0304-8853(99)00347-9

Krishnan KM, Pakhomov AB, Bao Y, Blomqvist P, Chun Y, Gonzales M, Griffin K, Ji X, Roberts BK (2006) Nanomagnetism and spin electronics: materials, microstructure and novel properties. J Mater Sci 41:793–815. doi:10.1007/s10853-006-6564-1

Li XG, Murai T, Saito T, Takahashi S (1998) Thermal stability, oxidation behavior and magnetic properties of Fe–Co ultrafine particles prepared by hydrogen plasma-metal reaction. J Magn Magn Mater 190:277–288. doi:10.1016/S0304-8853(98)00314-X

Li XG, Takahashi S, Watanabe K, Kikuchi Y, Koishi M (2001) Hybridization and characteristics of Fe and Fe–Co nanoparticles with polymer particles. Nano Lett 1:475–480. doi:10.1021/nl010007u

Li QL, Li HL, Pol VG, Bruckental I, Koltypin Y, Calderon-Moreno J, Nowik I, Gedanken A (2003) Sonochemical synthesis, structural and magnetic properties of air-stable Fe/Co alloy nanoparticles. New J Chem 27:1194–1199. doi:10.1039/b302136j

Liu LJ, Guan JG, Shi WD, Sun ZG, Zhao JS (2010) Facile synthesis and growth mechanism of flowerlike Ni–Fe alloy nanostructures. J Phys Chem C 114:13565–13570. doi:10.1021/jp104212v

Madsen MB, Mørup S (1986) Magnetic properties of ferrihydrite. Hyperfine Interact 27:329–332. doi:10.1007/BF02354773

Majetich S, Jin Y (1999) Magnetization directions of individual nanoparticles. Science 284:470–473. doi:10.1126/science.284.5413.470

Mazaleyrat F, Ammar M, LoBue M, Bonnet JP, Audebert P, Wang GY, Champion Y, Hytch M, Snoeck E (2009) Silica coated nanoparticles: synthesis, magnetic properties and spin structure. J Alloy Compd 483:473–478. doi:10.1016/j.jallcom.2008.08.121

Mørup S, Hansen MF (2007) Superparamagnetic particles. In: Kronmüller H, Parkin S (eds) Handbook of magnetism and advanced magnetic materials. Wiley-VCH, Weinheim

Naik SH, Carroll KJ, Carpenter EE (2011) Characterization of oxidation resistant Fe@M (M = Cr, Ni) core@shell nanoparticles prepared by a modified reverse micelle reaction. J Appl Phys 109:07B519. doi:10.1063/1.3548828

Nie Y, He HH, Gong RZ, Zhang XC (2007) The electromagnetic characteristics and design of mechanically alloyed Fe–Co particles for electromagnetic-wave absorber. J Magn Magn Mater 310:13–16. doi:10.1016/j.jmmm.2006.07.021

Nogues J, Sort J, Langlais V, Skumryev V, Surinach S, Munoz JS, Baro MD (2005) Exchange bias in nanostructures. Phys Rep Rev Sec Phys Lett 422:65–117. doi:10.1016/j.physrep.2005.08.004

Otsuka K, Yamamoto H, Yosizawa A (1984) Preparation of Fe, Co., and Ni ultrafine particles by hydrogen reduction of chloride vapors. Jpn J Chem 6:869–878

Pankhurst QA, Pollard RJ (1992) Structural and magnetic properties of ferrihydrite. Clay Clay Min 40:268–272. doi:10.1346/CCMN.1992.0400303

Pankhurst QA, Connolly J, Jones SK, Dobson J (2003) Applications of magnetic nanoparticles in biomedicine. J Phys D 36:R167–R181. doi:10.1088/0022-3727/36/13/201

Pardoe H, Chua-anusorn W, St. Pierre TG, Dobson J (2003) Detection limits for ferrimagnetic particle concentrations using magnetic resonance imaging based proton transverse relaxation rate measurements. Phys Med Biol 48:N89–N95. doi:10.1088/0031-9155/48/6/401

Poddar P, Wilson JL, Srikanth H, Ravi BG, Wachsmuth J, Sudarshan TS (2004) Grain size influence on soft ferromagnetic properties in Fe–Co nanoparticles. Mater Sci Eng B 106:95–100. doi:10.1016/j.mseb.2003.09.011

Rheinlander T, Kotitz R, Weitschies W, Semmler W (2000) Magnetic fractionation of magnetic fluids. J Magn Magn Mater 219:219–228. doi:10.1016/S0304-8853(00)00439-X

Shafi KVPM, Gedanken A, Goldfarb RB, Felner I (1997) Sonochemical preparation of nanosized amorphous Fe–Ni alloys. J Appl Phys 81:6901–6905. doi:10.1063/1.365250

Shen XQ, Guo LP, Liu MQ, Song FZ, Zhu YW (2011) A simple process for magnetic nanocrystalline porous Co–Fe alloy hollow microfibers. Mater Lett 65:17–18. doi:10.1016/j.matlet.2011.05.082

Sinfelt JH (1983) Bimetallic catalysts—discoveries, concepts, and applications. Wiley, New York

Skumryev V, Stoyanov S, Zhang Y, Hadjipanayis G, Givord D, Nogues J (2003) Beating the superparamagnetic limit with exchange bias. Nature 423:850–853. doi:10.1038/nature01687

Sugimoto M (1999) The past, present, and future of ferrites. J Am Ceram Soc 82:269–280. doi:10.1111/j.1551-2916.1999.tb20058.x

Suh YJ, Jang HD, Chang H, Kim WB, Kim HC (2006) Size-controlled synthesis of Fe–Ni alloy nanoparticles by hydrogen reduction of metal chlorides. Powder Technol 161:196–201. doi:10.1016/j.powtec.2005.11.002

Sun SH, Murray CB, Weller D, Folks L, Moser A (2000) Monodisperse FePt nanoparticles and ferromagnetic FePt nanocrystal superlattices. Science 287:1989–1992. doi:10.1126/science.287.5460.1989

Suresh G, Saravanan P, Babu DR (2011) Synthesis of Fe–Co nanobars using sodium sulfite assisted polyol process and their structural and magnetic studies. J Nano Res 15:21–28. doi:10.4028/www.scientific.net/JNanoR.15.21

Wang J, Zeng XC (2009) Core–shell magnetic nanoclusters. In: Liu JP, Fullerton E, Gutfleisch O, Sellmyer DJ (eds) Nanoscale magnetic materials and applications. Springer, Dordrecht, pp 35–66

Webb J, Macey DJ, Chua-anusorn W, St. Pierre TG, Brooker L, Rahman RI, Noller B (1999) Iron biominerals in medicine and the environment. Coord Chem Rev 190–192:1199–1215. doi:10.1016/S0010-8545(99)00176-9

Wertheim GK, Jaccarino V, Wernick JH, Buchanan DNE (1964) Range of the exchange interaction in iron alloys. Phys Rev Lett 12:24–27. doi:10.1103/PhysRevLett.12.24

Wu Z, Zhang M, Yu K, Zhang S, Xie Y (2008) Self-assembled double-shelled ferrihydrite hollow spheres with a tunable aperture. Chem Eur J 14:5346–5352. doi:10.1002/chem.200701945

Xu HM, Zhong W, Qi XS, Au CT, Deng Y, Du YW (2010) Highly stable Fe–Ni alloy nanoparticles encapsulated in carbon nanotubes: synthesis, structure and magnetic properties. J Alloy Compd 495:200–204. doi:10.1016/j.jallcom.2010.01.121